The Astrophysical Journal, 926:33 (9pp), 2022 February 10 https://doi.org/10.3847/1538-4357/ac397c

Four-year Cosmology Large Angular Scale Surveyor (CLASS) Observations: On-sky Receiver Performance at 40, 90, 150, and 220 GHz Frequency Bands

Sumit Dahal[1,2], John W. Appel[2], Rahul Datta[2], Michael K. Brewer[2], Aamir Ali[2,3], Charles L. Bennett[2], Ricardo Bustos[4], Manwei Chan[2], David T. Chuss[5], Joseph Cleary[2], Jullianna D. Couto[2], Kevin L. Denis[1], Rolando Dünner[6], Joseph Eimer[2], Francisco Espinoza[4], Thomas Essinger-Hileman[1,2], Joseph E. Golec[7], Kathleen Harrington[2,8], Kyle Helson[1,9], Jeffrey Iuliano[2], John Karakla[2], Yunyang Li (李云炀)[2], Tobias A. Marriage[2], Jeffrey J. McMahon[7,8], Nathan J. Miller[2], Sasha Novack[2], Carolina Núñez[2], Keisuke Osumi[2], Ivan L. Padilla[2], Gonzalo A. Palma[10], Lucas Parker[2,11], Matthew A. Petroff[2], Rodrigo Reeves[12], Gary Rhoades[2], Karwan Rostem[1], Deniz A. N. Valle[2], Duncan J. Watts[2,13], Janet L. Weiland[2], Edward J. Wollack[1], and Zhilei Xu (徐智磊)[2,14]

[1] NASA Goddard Space Flight Center, 8800 Greenbelt Road, Greenbelt, MD 20771, USA; sumit.dahal@nasa.gov
[2] Department of Physics and Astronomy, Johns Hopkins University, 3701 San Martin Drive, Baltimore, MD 21218, USA
[3] Department of Physics, University of California, Berkeley, CA 94720, USA
[4] Facultad de Ingeniería, Universidad Católica de la Santísima Concepción, Alonso de Ribera 2850, Concepción, Chile
[5] Department of Physics, Villanova University, 800 Lancaster Avenue, Villanova, PA 19085, USA
[6] Instituto de Astrofísica and Centro de Astro-Ingeniería, Facultad de Física, Pontificia Universidad Católica de Chile, Av. Vicuña Mackenna 4860, 7820436 Macul, Santiago, Chile
[7] Department of Physics, University of Chicago, Chicago, IL 60637, USA
[8] Department of Astronomy and Astrophysics, University of Chicago, 5640 South Ellis Avenue, Chicago, IL 60637, USA
[9] University of Maryland Baltimore County, 1000 Hilltop Circle, Baltimore, MD 21250, USA
[10] Departamento de Física, FCFM, Universidad de Chile, Blanco Encalada 2008, Santiago, Chile
[11] Space and Remote Sensing, MS D436, Los Alamos National Laboratory, Los Alamos, NM 87544, USA
[12] CePIA, Departamento de Astronomía, Universidad de Concepción, Concepción, Chile
[13] Institute of Theoretical Astrophysics, University of Oslo, P.O. Box 1029 Blindern, NO-0315 Oslo, Norway
[14] MIT Kavli Institute, Massachusetts Institute of Technology, 77 Massachusetts Avenue, Cambridge, MA 02139, USA

Received 2021 July 16; revised 2021 November 8; accepted 2021 November 12; published 2022 February 9

Abstract

The Cosmology Large Angular Scale Surveyor (CLASS) observes the polarized cosmic microwave background (CMB) over the angular scales of $1^\circ \lesssim \theta \leqslant 90^\circ$ with the aim of characterizing primordial gravitational waves and cosmic reionization. We report on the on-sky performance of the CLASS *Q*-band (40 GHz), *W*-band (90 GHz), and dichroic *G*-band (150/220 GHz) receivers that have been operational at the CLASS site in the Atacama desert since 2016 June, 2018 May, and 2019 September, respectively. We show that the noise-equivalent power measured by the detectors matches the expected noise model based on on-sky optical loading and lab-measured detector parameters. Using Moon, Venus, and Jupiter observations, we obtain power to antenna temperature calibrations and optical efficiencies for the telescopes. From the CMB survey data, we compute instantaneous array noise-equivalent-temperature sensitivities of 22, 19, 23, and 71 $\mu\mathrm{K_{cmb}}\sqrt{\mathrm{s}}$ for the 40, 90, 150, and 220 GHz frequency bands, respectively. These noise temperatures refer to white noise amplitudes, which contribute to sky maps at all angular scales. Future papers will assess additional noise sources impacting larger angular scales.

Unified Astronomy Thesaurus concepts: Cosmic microwave background radiation (322); Early universe (435); Observational cosmology (1146); Astronomical instrumentation (799); Polarimeters (1277); CMBR detectors (259)

1. Introduction

The cosmic microwave background (CMB) polarization is a unique probe to study the origin and evolution of the universe. The E-mode polarization component with $(-1)^\ell$ parity constrains the optical depth to reionization τ, which is currently the least constrained fundamental ΛCDM parameter (Bennett et al. 2013; Watts et al. 2018; Planck Collaboration VI 2020). This uncertainty in τ will be a limiting factor for improving constraints on the sum of neutrino masses from future CMB experiments (Abazajian et al. 2016). Additionally, the B-mode polarization component with $(-1)^{\ell+1}$ parity provides constraints on primordial gravitational waves (Kamionkowski et al. 1997; Seljak & Zaldarriaga 1997), which would provide evidence for inflation (Starobinskiĭ 1979; Guth 1981; Linde 1982). However, detecting primordial B-modes (if they in fact exist) is difficult in part because the B-mode signal is much fainter than the polarized Galactic foregrounds. The synchrotron emission from relativistic electrons accelerated in the Galactic magnetic field dominates at frequencies below ~70 GHz, while thermal emission from dust grains in the interstellar medium dominates at higher frequencies (Bennett et al. 2013; Watts et al. 2015; Planck Collaboration IV 2020). Therefore, it is necessary to pursue multifrequency observations for polarized foreground flux characterization and removal.

On small angular scales ($\theta \lesssim 1^\circ$), the conversion of brighter E-modes into B-modes through weak gravitational lensing by matter along the line of sight is an additional contaminant that needs to be well characterized, and has been measured by

Table 1
Summary of Median TES Bolometer Parameters

Parameter	Symbol [Unit]	40 GHz	90 GHz	150 GHz	220 GHz
Saturation Power	P_{sat} [pW]	6.3	18.4	35.0	43.8
Optical Loading[a]	P_γ [pW]	1.2	3.6	4.4	8.5
Optical Time Constant	τ_γ [ms]	3.4	2.1	1.5	1.4
Thermal Time Constant	τ_φ [ms]	17	7	8	6
Heat Capacity	C [pJ K^{-1}]	3	4	5	5
Responsivity	S [μA pW^{-1}]	−8.2	−2.9	−2.3	−2.2
Thermal Conductance	G [pW K^{-1}]	177	452	678	835
Thermal Conductance Constant	κ [nW K^{-4}]	13.4	24.9	18.9	21.8
Critical Temperature	T_{c} [mK]	149	167	205	209
Normal Resistance	R_{N} [mΩ]	8.2	11.0	13.8	13.9
Shunt Resistance	R_{sh} [$\mu\Omega$]	250	250	200	200
TES Loop Inductance	L [nH]	500	300	600	600

Note.
[a] The median precipitable water vapor (PWV) during the observing campaign was 1.0 mm for the 40 and 90 GHz arrays and 1.2 mm for the 150 and 220 GHz arrays.

multiple surveys (BICEP2 Collaboration et al. 2016; POLARBEAR Collaboration et al. 2017; Sherwin et al. 2017; Sayre et al. 2020). At large angular scales, the putative primordial B-mode signal has characteristic recombination and reionization peaks at $30 \lesssim \ell \lesssim 200$ and $\ell \lesssim 10$, respectively. Hence, measurements of the B-mode spectrum on larger than a degree angular scales ($\ell \lesssim 180$) not only help to minimize the contamination from lensing but also are essential to confirm the primordial origin of any potential signal measured at small angular scales. Currently, the tightest constraint on the amplitude of the gravitational waves parameterized through the tensor-to-scalar ratio $r < 0.036$ comes from combining the Planck and Wilkinson Microwave Anisotropy Probe (WMAP) data with the BICEP/Keck measurement of the recombination peak (Ade et al. 2021). Current experiments targeting the reionization peak include PIPER (Gandilo et al. 2016), QUIJOTE (López-Caniego et al. 2014), LSPE (Aiola et al. 2012), GroundBIRD (Tajima et al. 2012), and the Cosmology Large Angular Scale Surveyor (CLASS; Harrington et al. 2016).

CLASS maps the CMB polarization at multiple frequencies and targets both the recombination and reionization peaks from the Atacama desert with the aim of measuring a primordial B-mode signal at a sensitivity level of $r \sim 0.01$ and making a near cosmic-variance-limited measurement of τ (Essinger-Hileman et al. 2014; Watts et al. 2015, 2018; Harrington et al. 2016). The CLASS 40 GHz (*Q*-band) telescope (Eimer et al. 2012; Appel et al. 2014), which helps to measure foreground synchrotron emission, has been operational since 2016 June. The dichroic 150/220 GHz (*G*-band) receiver (Dahal et al. 2020), which aids in characterizing the polarized Galactic dust emission, started observations in 2019 September. CLASS is designed to be most sensitive at 90 GHz (*W* band) with two telescopes (Dahal et al. 2018; Iuliano et al. 2018) optimized for CMB observations near the minimum of polarized Galactic emission. The first *W*-band telescope has been operational since 2018 May, while the second is planned to be deployed in 2022. All four CLASS telescopes share a similar design (Eimer et al. 2012; Iuliano et al. 2018) with a variable-delay polarization modulator (VPM; Harrington et al. 2018) as the first optical element to place the signal band at ∼10 Hz, away from the low-frequency $1/f$ noise.

The CLASS *Q*-band on-sky performance, optical characterization, circular polarization sensitivity, and instrument stability based on the data taken between 2016 June and 2018 March ("Era 1") have already been published in a series of papers (Appel et al. 2019; Harrington et al. 2021; Padilla et al. 2020; Petroff et al. 2020; Xu et al. 2020). This paper presents the on-sky performance of the *Q*-band instrument after 2018 April ("Era 2") upgrades until 2020 March, and the *W*-band and *G*-band instruments from their respective deployments in 2018 May and 2019 September to 2020 March. The Era 2 data presented in this paper correspond to 636 days of observations for the *Q*-band (411 days with a grille filter installed; see Section 2.1), 611 days for the *W*-band, and 167 days for the *G*-band receivers. In Section 2, we describe the *Q*-band instrument upgrades and the *W*-band and *G*-band focal plane detector arrays. Section 3 shows the optical passband measurements and the on-sky optical loading extracted from *I*–*V* measurements. In Section 4, we report the noise performance based on the power spectral density (PSD) of the time-ordered data (TOD). Finally, in Section 5, we report the temperature calibrations of the instruments obtained from dedicated Moon/planet observations and the CMB sensitivities calculated from on-sky data for different CLASS detector arrays.

2. Focal Plane Arrays

The focal planes for all CLASS telescopes consist of smooth-walled feedhorns (Zeng et al. 2010) that couple light to polarization-sensitive transition-edge sensor (TES) bolometers through planar orthomode transducers (OMTs; Denis et al. 2009; Ade et al. 2009; Chuss et al. 2016; Rostem et al. 2016). Pulse-tube cooled dilution refrigerators (Iuliano et al. 2018) keep the bath temperature $\lesssim$60 mK, which is well below the superconducting transition temperature ($\gtrsim$150 mK) for CLASS TESs. These TESs are read out through superconducting quantum interference device (SQUID) amplifiers using time-division multiplexing (TDM; Reintsema et al. 2003; Battistelli et al. 2008).

Table 1 summarizes the median bolometer parameters for all four CLASS frequency bands. These parameters are based on *I*–*V* curves acquired by first ramping up the detector bias voltage (V) to drive the detectors normal and then stepping down the voltage while recording the current response (I) of the detectors. Saturation power (P_{sat}), thermal conductance (G), critical temperature (T_{c}), and normal resistance (R_{N}) were measured during dark lab tests by capping all of the cold stages of the cryostat with metal plates (Appel et al. 2014; Dahal et al. 2018, 2020). The optical loading (P_γ; see Section 3.2) and responsivity ($S = dI/dP_\gamma$) are estimated from on-sky I–V data. The optical time constant (τ_γ) is obtained by fitting detector TODs for a time constant that minimizes the hysteresis of the VPM signal synchronous with the grid−mirror distance (Appel et al. 2019; Harrington et al. 2021). The thermal time constant (τ_φ) is obtained by multiplying τ_γ with an electrothermal feedback speed-up factor estimated from I–V measurements, and the heat capacity (C) is the product of τ_φ and G measured for each detector.

2.1. Q-*band Upgrades*

The on-sky performance of the Q-band array from its deployment (2016 June) until 2018 March is described in detail in Appel et al. (2019). In 2018 April, we recovered eight detectors connected to a readout row that was damaged by an electrostatic discharge during deployment. The optically sensitive TESs connected to the broken readout channels were shifted to neighboring spare readout channels. After this fix we measure nominal I–V responses and successfully bias on transition all 72 optically sensitive TESs in the array. We found two irregular bolometers in the array: one with good optical efficiency but high noise ($\sim 10\times$ higher), and another with low optical efficiency (1%) but typical noise. We removed these from the analysis presented in this paper. These two detectors are not useful for mapping the sky but can be valuable in understanding and tracking systematic effects of the instrument.

During the Q-band instrument upgrade, we also replaced eight capacitive metal-mesh filters (MMFs; see Essinger-Hileman et al. 2014, Section 6.3) located at various cryogenic stages of the receiver with a stack of extruded polystyrene foam filters (Choi et al. 2013) at the 300 K stage. Transmission measurements of these MMFs fabricated by laser delamination of aluminized 12.6 μm polypropylene film yielded higher reflection coefficients than expected from transmission-line models (Ulrich 1967; Whitbourn & Compton 1985) and performance of similar filters produced using photolithography (Ade et al. 2006; Essinger-Hileman 2011). Two MMFs produced by photolithography of 6 μm mylar film coated with 30–50 nm of aluminum remain at the 60 K stage of the receiver. The replacement of the eight MMFs with foam filters did not affect the cryogenic performance of the receiver.

The on-sky optical efficiency after the upgrade was measured at 0.54, which is 12% higher than the 0.48 obtained from the first era of observations (Appel et al. 2019). The improved four-year absolute temperature calibration based on Venus and Jupiter observations (see Section 5.1) accounts for a 5% increase in our estimate of the instrument's optical efficiency. The additional 7% optical efficiency improvement is consistent with $\sim$1% in-band reflection per removed MMF. The in-band optical loading dropped from 1.6 to 1.2 pW even though the optical efficiency increased. This suggests the MMFs were coupling power onto the detectors from the 60 K cryostat walls and/or the 300 K optics cage. The increase in optical efficiency combined with lower optical loading improved the per-detector sensitivity by 30% from 258 $\mu\mathrm{K}\sqrt{\mathrm{s}}$ (Appel et al. 2019) to 180 $\mu\mathrm{K}\sqrt{\mathrm{s}}$ (Table 3).

The VPM control system was updated, and the baffle and cage enclosures were replaced to accommodate the Q-band and W-band receivers on a single mount. The new electromagnetic environment resulted in increased susceptibility of the Q-band receiver to radio-frequency (RF) noise, in particular to RF signals synchronous to the VPM controller. The W- and G-band detectors do not show similar sensitivity to the VPM RF signals. To improve the Q-band data quality and stability we installed a thin grille (TG) filter at the front of the vacuum window. The TG filter is a 0.51 mm thick brass plate with 5.25 mm diameter circular holes in a 5.75 mm pitch hexagonal packing. The TG filter greatly reduced detector RF noise, improving data quality at the cost of reducing optical efficiency to 0.43, while keeping the detector optical loading at 1.2 pW, and hence decreasing per-detector sensitivity to 217 $\mu\mathrm{K}\sqrt{\mathrm{s}}$. We are actively exploring TG designs with improved transmission that would return the receiver sensitivity to the benchmarks achieved with no TG filter installed. While the data with no TG filter installed was acquired between 2018 May and 2019 January, the remaining data from 2019 February until 2020 March were obtained with the TG filter installed.

2.2. W *Band*

The W-band instrument started observations at the CLASS site in 2018 May. The W-band focal plane contains seven identical modules, each consisting of 37 dual-polarization detectors fabricated on 100 mm silicon wafers (Rostem et al. 2016; Dahal et al. 2018). Each W-band pixel has two TES bolometers with each measuring the power in one of the two orthogonal linear polarization states. The total of 518 bolometers in the W-band focal plane are read out using 28 TDM columns, each multiplexing 22 rows of SQUIDs for a total of 616 readout channels. The remaining SQUID channels that are not connected to one of the 518 optically sensitive bolometers are either used to characterize readout noise and magnetic field pickup or are connected to a TES bolometer without optical coupling to monitor bath-temperature stability. These nonoptical bolometers are not considered for analysis in this paper; therefore, we will use "bolometers" to refer to only the optically sensitive bolometers.

Through in-lab characterization, we had reported in Dahal et al. (2018) that 426 out of 518 bolometers were functional (i.e., an array yield of 82%). During the deployment, we lost 19 bolometers on a single multiplexing row due to a failure in the readout. Out of the remaining 407 bolometers, we consider 319 that detect Venus at least 5 times (out of 74 observations) with signal-to-noise ratio (S/N) >3 and derived end-to-end optical efficiency greater than 5% (see Section 5.1) for further analysis in this paper. In addition to having a low optical efficiency, the lower yield of operable W-band detectors in the field can be mostly attributed to three coupled effects: (1) all 74 detectors within a module share a single bias line (compared to a maximum of 10 detectors per line for Q band and 44 for G band); (2) variations in detector properties within a wafer resulted in variations in their optimal bias points; and (3) a narrower stable bias range prevented accommodating variations in bias point (Effect 2) with a single bias line. We find that the G-band detectors (described in Section 2.3) do not suffer from the stability issue and can be biased down to $\lesssim 10\%\ R_\mathrm{N}$. Therefore, for the second W-band instrument, we have implemented various changes in the detector design to closely follow the G-band detector architecture (see Dahal et al. 2020, Figure 2). The new W-band detectors are being fabricated at the time of writing.

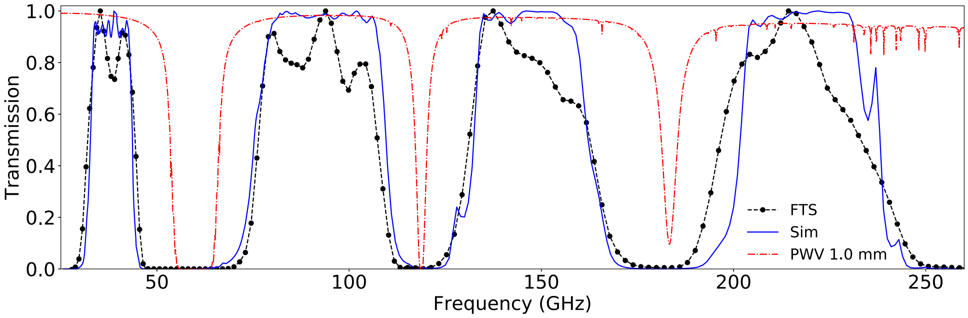

Figure 1. Average measured (dotted black) and simulated (solid blue) spectral response for different CLASS frequency bands overplotted with the atmospheric transmission model at the CLASS site with PWV = 1 mm (red dashed–dotted). The atmospheric transmission model was obtained from the Atacama Large Millimeter/submillimeter Array (ALMA) atmospheric transmission calculator based on the ATM code described in Pardo et al. (2001). The spectral response is normalized to unit peak, and the atmospheric transmission model is in units of fractional power transmitted. The bandwidths and center frequencies for different diffuse sources for these passbands are shown in Table 2.

2.3. G *Band*

The CLASS *G*-band instrument, which started observation in 2019 September, has a total of 255 dichroic dual-polarization pixels spread among three identical modules (Dahal et al. 2020). Each pixel contains four bolometers to simultaneously measure the two linear polarization states at 150 and 220 GHz frequency bands defined through on-chip filtering. These detectors are read out with 24 columns multiplexing 44 rows of SQUIDs. To optimize the detector biasing, each column is provided with a separate bias line. Before the deployment of the *G*-band instrument, we had reported array yields of 80% and 57% for the 150 and the 220 GHz frequency bands, respectively (Dahal et al. 2020). For 150 GHz, 389 out of 408 bolometers reported working in the lab detect Jupiter, and for 220 GHz, 211 out of 290 detect Jupiter. The larger difference for the 220 GHz detector array is mostly due to failure of two readout columns during deployment. For this paper, we conservatively exclude those *G*-band bolometers that detect Jupiter fewer than 5 times (out of 70 observations) with $S/N > 3$.

3. Optical Passband and Loading

A combination of absorptive, reflective, and scattering filters inside the receiver cryostat (Iuliano et al. 2018) suppresses the infrared power reaching the focal plane. Due to the details of the detector package geometry (Crowe et al. 2013), frequencies below the waveguide cutoff for each design and above the niobium gap energy (∼700 GHz) are suppressed. Between these frequencies, a series of broadband microstrip filters define the band edges and limit the out-of-band spectral response (U-yen & Wollack 2008; U-yen et al. 2008) for all CLASS detectors. The following subsections describe the measurements and show results for the passbands measured in the lab, and the in-band optical power measured in the field.

3.1. *Frequency Bands*

We measured the CLASS detector passbands using Martin–Puplett Fourier transform spectrometers (FTSs; Martin & Puplett 1970) in the lab. For the 40 and the 90 GHz detectors, a tabletop FTS made at the Johns Hopkins University with ∼1 GHz resolution (Wei 2012) was used to obtain the spectrum shown in Figure 1. The passband measurements and FTS testing setup for the 40 and the 90 GHz detectors are described in Appel et al. (2019) and Dahal et al. (2018), respectively. For the 150 and 220 GHz detectors, the lab cryostat and FTS testing setup did not allow the use of a tabletop FTS; therefore, a smaller and compact FTS with ∼2 GHz resolution (Pan et al. 2019) was used instead. Figure 1 shows measured and simulated CLASS passbands normalized to unit peak. The measured passbands have been corrected for the transmission through the lab cryostat filters and the frequency-dependent gain for the detector feedhorns that were placed a meter behind a 10 cm diameter cold stop. We co-added measured passbands from a subset of detectors with high S/N in each array to obtain the plot shown in Figure 1. The discrepancies observed in-band between measured and simulated passbands could be due to optical effects in the test setup not included in the simulation like FTS output, coupling between FTS and cryostat, and reflections inside the cryostat. However, the measurements show that all four passbands satisfy the design requirement to safely avoid strong atmospheric emission lines as shown in Figure 1.

It is worth noting that, compared to Figure 1, the passbands for the 150 and the 220 GHz detectors reported in Dahal et al. (2020) were shifted higher by a few GHz due to systematics associated with the compact FTS. The *G*-band measurements presented in Dahal et al. (2020) were performed with an FTS setup such that the plane with the wire-grid polarizers in the compact FTS (see Pan et al. 2019, Figure 1) was parallel to the vertical plane of the CLASS cryostat (Iuliano et al. 2018). As the FTS was rotated by 90° aligning the plane with the polarizers to the horizontal plane of the cryostat, the measured passbands shifted lower by a few GHz to produce the result shown in Figure 1. After the deployment of the *G*-band instrument, we investigated the FTS systematics in the lab to verify the accuracy of the measured passbands. We performed FTS measurements on spare 90 GHz CLASS detectors (nearly identical to the ones in the field) using a single-frequency HMC-C030[15] voltage-controlled oscillator (VCO) source. We tuned the VCO source to 7.5 GHz and used a ×12 frequency multiplier to produce 90 GHz input to the FTS optically coupled to the 90 GHz CLASS detectors inside the cryostat. While the vertical FTS configuration did not produce enough S/N output for the analysis, the horizontal configuration performed as expected showing a peak at 89.8 ± 1.0 GHz in response to the 90 GHz input. Therefore, we use FTS measurements from the horizontal configuration (Figure 1) for further *G*-band analysis in this paper.

---

[15] www.analog.com/products/hmc-c030

Table 2
Measured (and Simulated) Bandwidths and Effective Center Frequencies over CLASS Passbands (in GHz)

	Q Band	W Band	G Band (Lower)	G Band (Upper)
Bandwidths:				
FWHP	12.3 (10.9) ± 0.9	31.0 (34.3) ± 1.5	31.4 (29.7) ± 2.0	36.5 (36.4) ± 2.0
Dicke	14.0 (12.1) ± 0.9	34.4 (37.5) ± 1.5	37.6 (35.1) ± 2.0	47.0 (40.1) ± 2.0
Effective Center Frequencies[a]:				
Synchrotron	36.8 (37.2) ± 0.5	88.7 (88.9) ± 0.8	144.2 (145.2) ± 1.0	213.6 (217.4) ± 1.0
Rayleigh–Jeans	38.1 (38.1) ± 0.5	91.7 (92.5) ± 0.8	146.4 (147.2) ± 1.0	216.0 (219.1) ± 1.0
Dust	38.7 (38.5) ± 0.5	93.2 (94.2) ± 0.8	147.6 (148.1) ± 1.0	217.1 (220.0) ± 1.0
CMB	38.0 (38.1) ± 0.5	91.3 (92.0) ± 0.8	145.7 (146.6) ± 1.0	214.5 (218.0) ± 1.0

Note.
[a] The values are calculated over CLASS passbands for diffuse sources using Equation (2).

For all of the measured and simulated passbands, we calculate detector bandwidths in two different ways—full width at half power (FWHP) and Dicke bandwidth (Dicke 1946), which is defined as:

$$\Delta\nu_{\rm Dicke} \equiv \frac{\left[\int f(\nu)d\nu\right]^2}{\int f(\nu)^2 d\nu}, \tag{1}$$

where ν is the frequency and $f(\nu)$ is the spectral response. Following Page et al. (2003b), we also calculate the effective central frequencies for the measured passbands as:

$$\nu_{\rm e} \equiv \frac{\int \nu f(\nu)\sigma(\nu)d\nu}{\int f(\nu)\sigma(\nu)d\nu}, \tag{2}$$

where $\sigma(\nu)$ describes the frequency dependence for different sources. For a beam-filling Rayleigh–Jeans (RJ) source, the detector has a flat spectral response as the source spectrum is exactly canceled by the single-moded throughput; therefore, we set $\sigma(\nu) = 1$. For the diffuse synchrotron and dust sources, we use $\sigma(\nu) \propto \nu^{-3.1}$ and $\nu^{1.55}$, respectively (Planck Collaboration IV 2020). For the CMB, since the source measured is the anisotropy, we set:

$$\sigma(\nu) \propto \frac{1}{\nu^2}\frac{\partial B(\nu,\,T)}{\partial T}\bigg|_{T=T_{\rm cmb}} \propto \frac{\nu^2 e^x}{(e^x-1)^2}, \tag{3}$$

where $B(\nu,\,T)$ is the Planck blackbody, $T_{\rm cmb} = 2.725$ K, and $x = h\nu/kT_{\rm cmb}$, where h and k are the Planck and the Boltzmann constants, respectively. The calculated bandwidths and effective central frequencies for all of these diffuse sources for both the measured and the simulated passbands are tabulated in Table 2. The associated uncertainties are the quadrature summations of the respective standard errors on the mean and their measurement resolutions (full FTS resolution for bandwidths and half the resolution for effective center frequencies). The latter dominates the quoted uncertainties for all four frequency bands.

3.2. Optical Loading

The CLASS observation strategy is to scan azimuthally across 720° at a constant elevation of 45° (Xu et al. 2020). The telescope boresight angle is changed by 15° once per 24 hr observing cycle, nominally covering seven boresight angles from −45° to +45° each week. At the beginning of the observing cycle for the day, we acquire I–V curves to select the optimal detector bias voltage. For W band, we apply one voltage bias per module (i.e., four columns), whereas for Q and G bands, we choose one bias per column. Using the I–V data, we measure the detector bias power ($P_{\rm bias}$) defined as $P_{\rm bias} = I \times V$ at 80% $R_{\rm N}$. The detector optical loading P_γ can then be calculated by subtracting this $P_{\rm bias}$ from the detector saturation power $P_{\rm sat}$ calculated during dark lab tests, i.e., $P_\gamma = P_{\rm sat} - P_{\rm bias}$. We show the spread of array-averaged P_γ for all four frequency bands during the Era 2 observing campaign in Figure 2. The range of measured optical loading narrows substantially at the lower-frequency bands, highlighting the stability of the atmospheric emission at the CLASS site. The prominent atmospheric features near the CLASS frequency bands are the 60 and 117 GHz oxygen emission lines and the 183 GHz water emission line (Figure 1). Therefore, due to their proximity to the water line, the loading at the higher-frequency bands increases with the precipitable water vapor (PWV) levels. Since the Q band is the furthest away from the 183 GHz water line, its loading is least sensitive to weather variations as the oxygen emission remains relatively constant. The median array-averaged loading P_γ during the observing campaign for the 40, 90, 150, and 220 GHz detector arrays were 1.2, 3.6, 4.4, and 8.5 pW, respectively. Note that while Figure 2 shows the data for the 40 GHz instrument with the TG filter installed, the median loading without the filter was the same.

4. Noise Performance

CLASS detectors are background limited, meaning that the optical loading drives the total detector noise measured. For a given P_γ, the noise-equivalent power (NEP) for a detector can be modeled as:

$$\text{NEP}^2 = \text{NEP}_{\rm d}^2 + h\nu_0 P_\gamma + \frac{P_\gamma^2}{\Delta\nu}, \tag{4}$$

where $\text{NEP}_{\rm d}$ is the dark detector noise, h is the Planck constant, and ν_0 and $\Delta\nu$ are the detector center frequency and bandwidth, respectively. In Figure 2, we compare the measured NEP from on-sky data to the NEP model from Equation (4) for all four CLASS frequency bands. For the NEP model, we use lab-measured RJ center frequencies and FWHP bandwidths from Table 2, and $\text{NEP}_{\rm d}$ of 11 ± 1 aW $\sqrt{\rm s}$ (Appel et al. 2014), 24 ± 5 aW $\sqrt{\rm s}$ (Dahal et al. 2018), 22 ± 4 aW $\sqrt{\rm s}$, and 25 ± 4 aW $\sqrt{\rm s}$ (Dahal et al. 2020) for the 40, 90, 150, and 220 GHz arrays, respectively. The model uncertainty is based on the errors measured in these parameters. The measured NEP values are computed from the

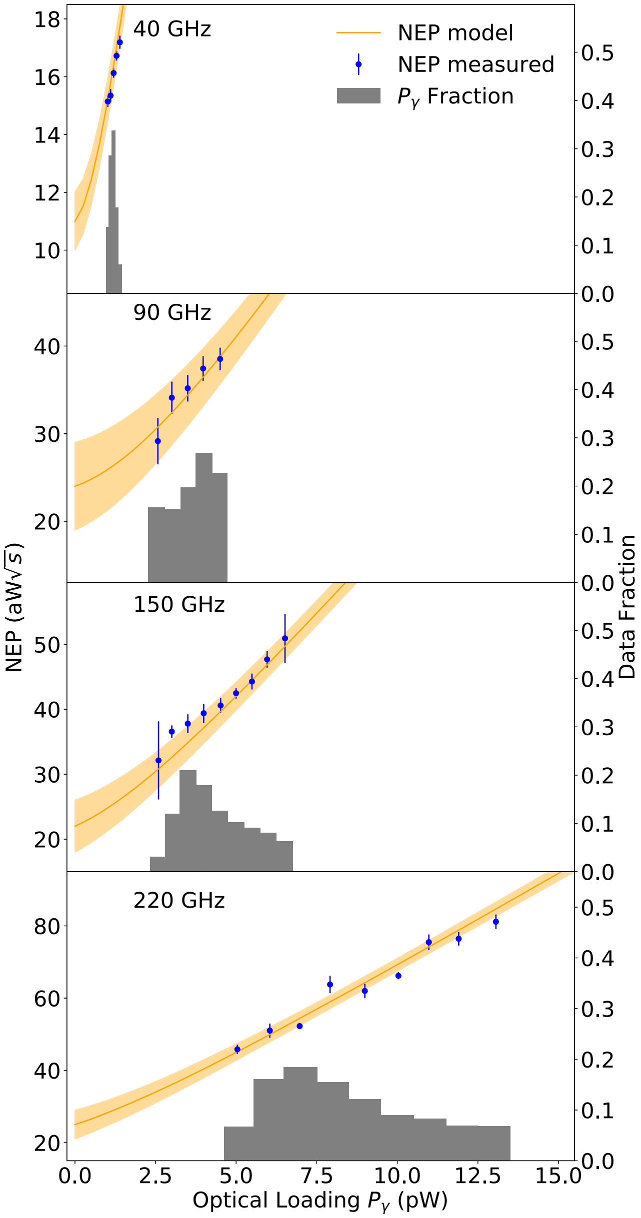

Figure 2. Array-averaged NEP vs. P_γ for different CLASS frequency bands. The blue points are the measured values from CMB survey scans whereas the orange curves are noise-equivalent power (NEP) models (Equation (4)) based on lab-measured detector parameters. The error bars on the data points and the shaded regions around the models are the 1σ uncertainties. Before binning the measured NEP values, a data selection cut of wind speed <1.5 m s^{-1} was applied for all four detector arrays. The histograms show the spread of array-averaged P_γ measured during the entire Era 2 observing campaign. The measured NEP values from CMB scans are consistent with the models at all four frequency bands.

PSD of pair-differenced 10 minutes TODs obtained from on-sky observations. First, we subtract detector TODs from each polarization pair within a pixel to reduce any correlated noise. Then, we take the average of the PSD in the side-bands of the 10 Hz modulation frequency, and divide the average by two to recover the per-detector NEP. For all four detector arrays, we average the PSDs over the side-bands of 8.0–9.0 and 11.0–12.0 Hz.

Figure 2 shows the binned pair-differenced NEP averaged across the array versus the average P_γ for all four CLASS frequency bands. Since the P_γ values are based on the *I–V* measurements and we only acquire *I–V* data once per day during nominal CMB scans, we only bin the NEP values from the TODs acquired within four hours after an *I–V* is acquired. This is especially important for the *G*-band detectors as they can have larger variations in the atmospheric loading throughout the day. It is also worth noting that although single detectors without an operational pair were not included in this analysis, they could still be mapped for the CMB analysis.

Before binning the NEP versus P_γ values shown in Figure 2, we applied a data selection cut for all four detector arrays to remove the TODs acquired when the wind speed at the site was higher than 1.5 m s^{-1}. The effect of high wind speeds on CLASS data is discussed in Harrington et al. (2021) and will be explored further in upcoming publications. In Section 5.2, we compute the overall sensitivity for all CLASS detector arrays without applying any wind speed cuts to the TODs. For Figure 2, a wind speed <1.5 m s^{-1} data selection cut was applied to compare the data to the detector NEP model.

For all four frequency bands, the on-sky measured NEP values are consistent with the NEP models based on lab-measured parameters as shown in Figure 2. The measured NEPs are dominated by photon bunching (third term in Equation (4)) and verify that the CLASS detectors are background limited at all four frequency bands, as designed. Compared to Era 1 observations (see Appel et al. 2019, Figure 3), the NEP for 40 GHz detectors decreased by ∼21%, primarily due to lower optical loading achieved through the *Q*-band instrument upgrade (Section 2.1).

5. Moon and Planet Observations

CLASS periodically performs dedicated observations of the Moon, Venus, and Jupiter to calibrate the detectors' power response, obtain telescope pointing information, and characterize the beam response. During these dedicated observations, the telescopes scan across the source azimuthally at a fixed elevation as the source rises or sets through the telescopes' fields of view. Since the Moon provides the highest S/N, it is used to obtain pointing information (Xu et al. 2020) for all CLASS telescopes. However, it saturates the *W*-band and *G*-band detectors, and its absolute *Q*-band brightness temperature is not well established. Therefore, when available, we use Venus and/or Jupiter observations to obtain detector calibration from measured power to antenna temperature of the source.

During Era 2, all three CLASS telescopes performed 70 dedicated Jupiter observations. In addition, the *Q*- and *W*-band telescopes performed 74 dedicated Venus scans. Since the *G*-band receiver was deployed, Venus has not been available for observations. Therefore, for the detector calibration summarized in Section 5.1, we use Jupiter observations for 150 and 220 GHz detectors whereas we use average values obtained from both Venus and Jupiter for 40 and 90 GHz detectors. After the TG filter was installed in the *Q*-band instrument, neither planet has been available for observations; hence we use Moon observations instead for this particular configuration.

5.1. Calibration to Antenna Temperature

Given the telescope beam sizes (see Table 3), both planets (and the Moon for *Q* band) are well approximated as "point sources" whose brightness temperature (T_{p}) relates to the peak

Table 3
Optical Performance Summary (Array Medians) of CLASS Telescopes

Parameter	Symbol [Unit]	40 GHz[a]	90 GHz	150 GHz	220 GHz
Beam FWHM	θ [arcmin]	95	37	23	16
Beam Solid Angle	Ω [μsr]	822	136	51	26
Telescope Efficiency	η	0.54 (0.43)	0.42	0.45	0.45
RJ Temperature Calibration	$\frac{dT_{\rm RJ}}{dP_\gamma}$ [K pW^{-1}]	10.8 (13.8)	5.5	5.1	4.4
CMB−RJ Calibration	$\frac{dT_{\rm cmb}}{dT_{\rm RJ}}$	1.04	1.23	1.68	2.92
Detector Dark Noise Power	$\mathrm{NEP_d}$ [aW $\sqrt{s}$]	11	24	22	25
Detector Total Noise Power	NEP [aW $\sqrt{s}$]	16 (15)	47	51	83
Detector Noise Temperature	NET [$\mu\mathrm{K_{cmb}}\sqrt{s}$]	180 (217)	346	453	1034
No. of Optical Detectors	$N_{\rm det}$	70	319	389	211
Array Noise Temperature	$\mathrm{NET_{array}}$ [$\mu\mathrm{K_{cmb}}\sqrt{s}$]	22 (26)	19	23	71

Note.
[a] The 40 GHz optical performance after 2018 April upgrade. The values in parentheses correspond to the telescope's performance with the TG filter installed.

response measured by CLASS detectors ($T_{\rm m}$) as:

$$T_{\rm p}\Omega_{\rm p} = T_{\rm m}\Omega_{\rm B}, \tag{5}$$

where $\Omega_{\rm B}$ is the beam solid angle and $\Omega_{\rm p}$ is the solid angle subtended by the source (Page et al. 2003a). For *W*- and *G*-band detectors, $T_{\rm m}$ is also corrected for atmospheric transmission to account for the effect of PWV at the CLASS site. We calculate the correction factor using the PWV data from APEX[16] and ACT (Bustos et al. 2014) radiometers along with the atmospheric transmission model based on Pardo et al. (2001) shown in Figure 1. No correction was necessary for the *Q*-band detectors as the effect of PWV on $T_{\rm m}$ was less than a percent.

For a given CLASS detector, the calibration factor from power deposited on the bolometer dP_γ to antenna (RJ) temperature on the sky $dT_{\rm RJ}$ can now be written as:

$$\frac{dT_{\rm RJ}}{dP_\gamma} = \frac{T_{\rm m}}{P_0} = \frac{T_{\rm p}}{P_0}\frac{\Omega_{\rm p}}{\Omega_{\rm B}}, \tag{6}$$

where P_0 is the peak power amplitude measured by the bolometer. For Jupiter observations, we use $T_{\rm p} = 152.6 \pm 0.6$ K,[17] 172.8 ± 0.5 K (Bennett et al. 2013), 174.1 ± 0.9 K, and 175.8 ± 1.1 K (Planck Collaboration Int. LII., 2017) for the 40, 90, 150, and 220 GHz detectors, respectively. For Venus observations, we use $T_{\rm p} = 430.4 \pm 2.8$ K for 40 GHz and 354.5 ± 1.3 K for 90 GHz from Dahal et al. (2021).[18] For the 40 GHz Moon observations used to calibrate the TG filter configuration, we use $T_{\rm p} = 200 \pm 1$ K. Following a similar procedure to that described in Dahal et al. (2021), this value was obtained by comparing Moon to Jupiter observations performed when the TG filter was not in place.

Finally, we obtain per-detector $dT_{\rm RJ}/dP_\gamma$ values by averaging all of the individual observations of a source acquired throughout the observing campaign. This per-detector averaging is performed on a map level (Xu et al. 2020). For every dedicated planet/Moon observation, a source-centered map is produced using the TOD and telescope pointing information for a given detector. The individual maps are then averaged to form an aggregate map of the source from which P_0 and $\Omega_{\rm B}$ values for Equation (6) are extracted. Since $\Omega_{\rm p}$ changes between observations, the detector response is scaled by $1/\Omega_{\rm p}$ while averaging the maps. While $\Omega_{\rm p}$ of all three sources vary with the changing distance between the source and CLASS telescopes, $\Omega_{\rm p}$ of Jupiter also varies with time due to changes in viewing angle for the oblate planet. We correct for this Jupiter disk oblateness using the method described in Weiland et al. (2011). In addition, for the *Q*-band Moon observations, the detector response is scaled by $\langle T_{\rm model}\rangle/T_{\rm model}$, where $T_{\rm model}$ is a phase-dependent disk-averaged Moon brightness temperature model (Xu et al. 2020) derived from the Chang'E 37 GHz data (Zheng et al. 2012) and $\langle T_{\rm model}\rangle$ is the model brightness temperature averaged over all Moon phases.

Table 3 shows the array median $dT_{\rm RJ}/dP_\gamma$ calibration factors for all four CLASS frequency bands. These calibration factors relate to the telescopes' optical efficiency (η) as follows:

$$\begin{aligned}\eta &= \left(k\Delta\nu\frac{dT_{\rm RJ}}{dP_\gamma}\right)^{-1}\\ &= 0.54^{+0.05}_{-0.03}\ (40\ \text{GHz w/o TG})\\ &= 0.43^{+0.03}_{-0.03}\ (40\ \text{GHz w/ TG})\\ &= 0.42^{+0.15}_{-0.22}\ (90\ \text{GHz})\\ &= 0.45^{+0.05}_{-0.06}\ (150\ \text{GHz})\\ &= 0.45^{+0.05}_{-0.04}\ (220\ \text{GHz}),\end{aligned} \tag{7}$$

where k is the Boltzmann constant and $\Delta\nu$ is the detector bandwidth (measured FWHP) from Table 2. The values in Equation (7) are array medians, and the uncertainties indicate 68% widths of the respective distributions. Figure 3 shows the distribution of η for all four CLASS frequency bands. Compared to Era 1 of CLASS observations (Appel et al. 2019), we achieved a $\sim$7% higher optical efficiency at 40 GHz (without TG filter) by removing the MMFs from the *Q*-band receiver (Section 2.1). The median optical efficiencies achieved by 90, 150, and 220 GHz detector arrays are similar to that of the 40 GHz array in Era 1. For the 90 GHz array, while some detectors have efficiencies similar to that of the other frequency

---

[16] https://archive.eso.org/wdb/wdb/asm/meteo_apex/form

[17] Considering the steep Jupiter spectrum at *Q* band, we use a local power-law fit between WMAP's *Ka* and *Q*-band measurements to correct for the $\sim$2 GHz difference in effective center frequencies between WMAP and CLASS *Q*-band detectors.

[18] We note that these Venus brightness temperature values were obtained from a separate analysis using CLASS data and WMAP-measured Jupiter brightness temperatures. Refer to Dahal et al. (2021) for details.

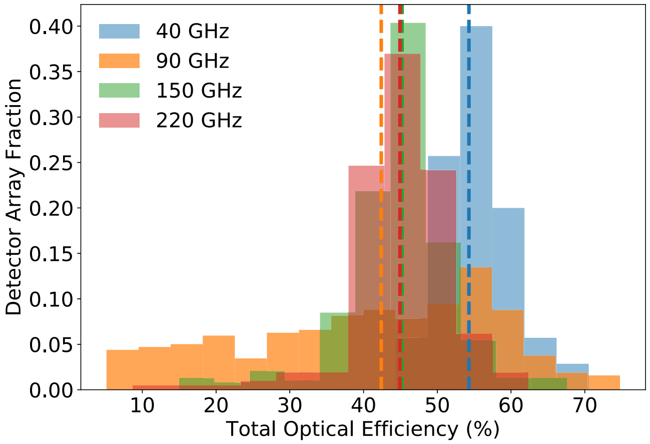

Figure 3. The distribution of end-to-end (detector plus telescope optics) optical efficiency for CLASS detector arrays obtained from planet observations. The dashed lines represent the array medians, and the array fraction is based on the total number of optically sensitive detectors ($N_{\rm det}$ in Table 3) in a given array. The 40 GHz efficiency values shown here were obtained after the 2018 April receiver upgrade and without the TG filter installed; the TG filter lowers the median efficiency to 43%.

bands, the spread is large and skewed toward low efficiency as shown in Figure 3. We are actively investigating the cause of this larger efficiency spread by revisiting the design of the *W*-band detector components.

5.2. CMB Sensitivity

The antenna temperature $dT_{\rm RJ}$ can be converted to the CMB thermodynamic temperature $dT_{\rm cmb}$ as:

$$\frac{dT_{\rm cmb}}{dT_{\rm RJ}} \approx \frac{(e^{x_0}-1)^2}{x_0^2\, e^{x_0}}, \tag{8}$$

where $x_0 = h\nu_0/kT_{\rm cmb}$ and ν_0 is the CMB center frequency from Table 2. Combining Equations (6) and (8), we can calculate the calibration factor from dP_γ to $dT_{\rm cmb}$ as follows:

$$\begin{aligned}\frac{dT_{\rm cmb}}{dP_\gamma} &= \frac{dT_{\rm cmb}}{dT_{\rm RJ}}\frac{dT_{\rm RJ}}{dP_\gamma}\\ &= 11.3^{+0.7}_{-0.9}\ {\rm K\ pW^{-1}}\ (40\ {\rm GHz\ w/o\ TG})\\ &= 14.4^{+1.3}_{-1.0}\ {\rm K\ pW^{-1}}\ (40\ {\rm GHz\ w/TG})\\ &= 6.8^{+7.7}_{-1.8}\ {\rm K\ pW^{-1}}\ (90\ {\rm GHz})\\ &= 8.6^{+1.3}_{-0.9}\ {\rm K\ pW^{-1}}\ (150\ {\rm GHz})\\ &= 12.9^{+1.3}_{-1.3}\ {\rm K\ pW^{-1}}\ (220\ {\rm GHz}),\end{aligned} \tag{9}$$

where the values are array medians, and the uncertainties are 68% widths of the respective distributions. While we intend to calibrate the CLASS CMB maps through cross-correlation with maps from WMAP and Planck, the $dT_{\rm cmb}/dP_\gamma$ in Equation (9) obtained from the planets/Moon can be used to check CLASS noise modeling to achieve additional constraints on experiment characterization.

Multiplying the per-detector $dT_{\rm cmb}/dP_\gamma$ by the NEP values (Section 4) gives the detector's CMB sensitivity in terms of noise-equivalent temperature (NET). For every detector, we first calculate a median NEP from all of the 10 minutes TODs acquired throughout the observing campaign. Using the per-detector median NEP and $dT_{\rm cmb}/dP_\gamma$, we obtain the detector NET values, which are summarized in Table 3. Finally, we calculate the array noise temperatures by inverse-variance weighting the NETs of all of the optically sensitive detectors in a given array. These array noise temperatures presented in Table 3 represent instantaneous array sensitivities achieved by CLASS telescopes during the Era 2 observing campaign. In terms of sky maps, these noise temperatures refer to white noise amplitudes, which contribute to maps at all angular scales. Future publications will assess additional noise sources impacting larger angular scales.

6. Conclusion

We have presented the on-sky performance of the CLASS receivers at 40, 90, 150, and 220 GHz frequency bands based on data acquired during the Era 2 observing campaign between 2018 April and 2020 March. In this paper, we summarize the measured detector parameters including optical loading, time constants, and passbands, and verify that the on-sky NEP measurements are consistent with expected detector noise models. Using the Moon, Venus, and Jupiter as calibrators, we obtain the end-to-end optical efficiency and measured power to antenna temperature calibration for all of the optically sensitive detectors. These measurements imply instantaneous array sensitivities of 22, 19, 23, and 71 $\mu{\rm K_{cmb}}\sqrt{\rm s}$ for the 40, 90, 150, and 220 GHz detector arrays, respectively. As a result of the instrument upgrade, the 40 GHz telescope is now ~31% more sensitive than it was during Era 1 observations (Appel et al. 2019). The addition of a second 90 GHz instrument will further increase CLASS's CMB sensitivity near the minimum of polarized Galactic emission.

This paper is a part of a series of publications on the CLASS Era 2 multifrequency observations. Upcoming publications will address beam profile, polarization performance, and science results.

We acknowledge the National Science Foundation Division of Astronomical Sciences for their support of CLASS under grant Nos. 0959349, 1429236, 1636634, 1654494, and 2034400. We thank Johns Hopkins University President R. Daniels and the Deans of the Kreiger School of Arts and Sciences for their steadfast support of CLASS. We further acknowledge the very generous support of Jim and Heather Murren (JHU A&S '88), Matthew Polk (JHU A&S Physics BS '71), David Nicholson, and Michael Bloomberg (JHU Engineering '64). The CLASS project employs detector technology developed in collaboration between JHU and Goddard Space Flight Center under several previous and ongoing NASA grants. Detector development work at JHU was funded by NASA cooperative agreement 80NSSC19M0005. CLASS is located in the Parque Astronómico Atacama in northern Chile under the auspices of the Agencia Nacional de Investigación y Desarrollo (ANID).

We acknowledge scientific and engineering contributions from Max Abitbol, Fletcher Boone, Lance Corbett, David Carcamo, Mauricio Díaz, Pedro Fluxa, Dominik Gothe, Ted Grunberg, Mark Halpern, Saianeesh Haridas, Connor Henley, Gene Hilton, Johannes Hubmayr, Ben Keller, Lindsay Lowry, Nick Mehrle, Grace Mumby, Diva Parekh, Bastian Pradenas, Isu Ravi, Carl Reintsema, Daniel Swartz, Emily Wagner, Bingjie Wang, Qinan Wang, Tiffany Wei, Ziáng Yan, Lingzhen Zeng, and Zhuo Zhang. For essential logistical support, we thank Jill Hanson, William Deysher, Miguel Angel Díaz, María José Amaral, and Chantal Boisvert. We acknowledge productive collaboration with Dean Carpenter and the JHU Physical Sciences Machine Shop team.

S.D. is supported by an appointment to the NASA Postdoctoral Program at the NASA Goddard Space Flight Center, administered by Universities Space Research Association under contract with NASA. S.D. acknowledges support under NASA–JHU Cooperative Agreement 80NSSC19M005. K.H. is supported by NASA under award number 80GSFC17M0002. R.R. acknowledges partial support from CATA, BASAL grant AFB-170002, and CONICYT-FONDECYT through grant 1181620. Z.X. is supported by the Gordon and Betty Moore Foundation.

Software: `PyEphem` (Rhodes 2011), `NumPy` (van der Walt et al. 2011), `SciPy` (Virtanen et al. 2020), `Astropy` (Astropy Collaboration et al. 2013), `Matplotlib` (Hunter 2007).

ORCID iDs

Sumit Dahal https://orcid.org/0000-0002-1708-5464
John W. Appel https://orcid.org/0000-0002-8412-630X
Rahul Datta https://orcid.org/0000-0003-3853-8757
Aamir Ali https://orcid.org/0000-0001-7941-9602
Charles L. Bennett https://orcid.org/0000-0001-8839-7206
Ricardo Bustos https://orcid.org/0000-0001-8468-9391
David T. Chuss https://orcid.org/0000-0003-0016-0533
Jullianna D. Couto https://orcid.org/0000-0002-0552-3754
Rolando Dünner https://orcid.org/0000-0003-3892-1860
Joseph Eimer https://orcid.org/0000-0001-6976-180X
https://orcid.org/0000-0002-4782-3851
Kathleen Harrington https://orcid.org/0000-0003-1248-9563
Kyle Helson https://orcid.org/0000-0001-9238-4918
Yunyang Li (李云炀) https://orcid.org/0000-0002-4820-1122
Tobias A. Marriage https://orcid.org/0000-0003-4496-6520
Jeffrey J. McMahon https://orcid.org/0000-0001-7466-0317
Nathan J. Miller https://orcid.org/0000-0002-2245-1027
Carolina Núñez https://orcid.org/0000-0002-5247-2523
Keisuke Osumi https://orcid.org/0000-0003-2838-1880
Ivan L. Padilla https://orcid.org/0000-0002-0024-2662
Gonzalo A. Palma https://orcid.org/0000-0002-5890-9554
Lucas Parker https://orcid.org/0000-0002-8224-859X
Matthew A. Petroff https://orcid.org/0000-0002-4436-4215
Rodrigo Reeves https://orcid.org/0000-0001-5704-271X
Karwan Rostem https://orcid.org/0000-0003-4189-0700
Deniz A. N. Valle https://orcid.org/0000-0003-3487-2811
Duncan J. Watts https://orcid.org/0000-0002-5437-6121
Janet L. Weiland https://orcid.org/0000-0003-3017-3474
Edward J. Wollack https://orcid.org/0000-0002-7567-4451
Zhilei Xu (徐智磊) https://orcid.org/0000-0001-5112-2567

References

Abazajian, K. N., Adshead, P., Ahmed, Z., et al. 2016, arXiv:1610.02743
Ade, P. A. R., Ahmed, Z., Amiri, M., et al. 2021, PhRvL, 127, 151301
Ade, P. A. R., Chuss, D. T., Hanany, S., et al. 2009, JPhCS, 155, 012006
Ade, P. A. R., Pisano, G., Tucker, C., & Weaver, S. 2006, Proc. SPIE, 6275, 62750U
Aiola, S., Amico, G., Battaglia, P., et al. 2012, Proc. SPIE, 8446, 84467A
Appel, J. W., Ali, A., Amiri, M., et al. 2014, Proc. SPIE, 9153, 91531J
Appel, J. W., Xu, Z., Padilla, I. L., et al. 2019, ApJ, 876, 126
Astropy Collaboration, Robitaille, T. P., Tollerud, E. J., et al. 2013, A&A, 558, A33
Battistelli, E. S., Amiri, M., Burger, B., et al. 2008, JLTP, 151, 908
Bennett, C. L., Larson, D., Weiland, J. L., et al. 2013, ApJS, 208, 20
BICEP2 Collaboration, Keck Array Collaboration, Ade, P. A. R., et al. 2016, ApJ, 833, 228
Bustos, R., Rubio, M., Otárola, A., & Nagar, N. 2014, PASP, 126, 1126
Choi, J., Ishitsuka, H., Mima, S., et al. 2013, RScI, 84, 114502
Chuss, D. T., Ali, A., Amiri, M., et al. 2016, JLTP, 184, 759
Crowe, E. J., Bennett, C. L., Chuss, D. T., et al. 2013, ITAS, 23, 2500505
Dahal, S., Ali, A., Appel, J. W., et al. 2018, Proc. SPIE, 10708, 107081Y
Dahal, S., Amiri, M., Appel, J. W., et al. 2020, JLTP, 199, 289
Dahal, S., Brewer, M. K., Appel, J. W., et al. 2021, PSJ, 2, 71
Denis, K. L., Cao, N. T., Chuss, D. T., et al. 2009, in AIP Conf. Proc. 1185, 13th Int. Workshop on Low Temperature Detectors - LTD13 (Melville, NY: AIP), 371
Dicke, R. H. 1946, RScI, 17, 268
Eimer, J. R., Bennett, C. L., Chuss, D. T., et al. 2012, Proc. SPIE, 8452, 845220
Essinger-Hileman, T. 2011, PhD thesis, Princeton University
Essinger-Hileman, T., Ali, A., Amiri, M., et al. 2014, Proc. SPIE, 9153, 91531I
Gandilo, N. N., Ade, P. A. R., Benford, D., et al. 2016, Proc. SPIE, 9914, 99141J
Guth, A. H. 1981, PhRvD, 23, 347
Harrington, K., Datta, R., Osumi, K., et al. 2021, ApJ, 922, 212
Harrington, K., Eimer, J., Chuss, D. T., et al. 2018, Proc. SPIE, 10708, 107082M
Harrington, K., Marriage, T., Ali, A., et al. 2016, Proc. SPIE, 9914, 99141K
Hunter, J. D. 2007, CSE, 9, 90
Iuliano, J., Eimer, J., Parker, L., et al. 2018, Proc. SPIE, 10708, 1070828
Kamionkowski, M., Kosowsky, A., & Stebbins, A. 1997, PhRvD, 55, 7368
Linde, A. D. 1982, PhLB, 108, 389
López-Caniego, M., Rebolo, R., Aguiar, M., et al. 2014, arXiv:1401.4690
Martin, D. H., & Puplett, E. 1970, InfPh, 10, 105
Padilla, I. L., Eimer, J. R., Li, Y., et al. 2020, ApJ, 889, 105
Page, L., Barnes, C., Hinshaw, G., et al. 2003a, ApJS, 148, 39
Page, L., Jackson, C., Barnes, C., et al. 2003b, ApJ, 585, 566
Pan, Z., Liu, M., Basu Thakur, R., et al. 2019, ApOpt, 58, 6257
Pardo, J. R., Cernicharo, J., & Serabyn, E. 2001, ITAP, 49, 1683
Petroff, M. A., Eimer, J. R., Harrington, K., et al. 2020, ApJ, 889, 120
Planck Collaboration Int. LII. 2017, A&A, 607, A122
Planck Collaboration IV 2020, A&A, 641, A4
Planck Collaboration VI 2020, A&A, 641, A6
POLARBEAR Collaboration, Ade, P. A. R., Aguilar, M., et al. 2017, ApJ, 848, 121
Reintsema, C. D., Beyer, J., Nam, S. W., et al. 2003, RScI, 74, 4500
Rhodes, B. C. 2011, PyEphem: Astronomical Ephemeris for Python, Astrophysics Source Code Library, ascl:1112.014
Rostem, K., Ali, A., Appel, J. W., et al. 2016, Proc. SPIE, 9914, 99140D
Sayre, J. T., Reichardt, C. L., Henning, J. W., et al. 2020, PhRvD, 101, 122003
Seljak, U., & Zaldarriaga, M. 1997, PhRvL, 78, 2054
Sherwin, B. D., van Engelen, A., Sehgal, N., et al. 2017, PhRvD, 95, 123529
Starobinskiĭ, A. A. 1979, JETPL, 30, 682
Tajima, O., Choi, J., Hazumi, M., et al. 2012, Proc. SPIE, 8452, 84521M
Ulrich, R. 1967, InfPh, 7, 37
U-yen, K., Chuss, D., & Wollack, E. J. 2008, in CMB Polarization Technology Workshop: Technology Development for a CMB Probe of Inflation, ed. S. Hanany (Boulder, CO: Kavli Institute for Cosmological Physics)
U-yen, K., & Wollack, E. J. 2008, in 2008 38th European Microwave Conf. (Piscataway, NJ: IEEE), 642
van der Walt, S., Colbert, S. C., & Varoquaux, G. 2011, CSE, 13, 22
Virtanen, P., Gommers, R., Oliphant, T. E., et al. 2020, NatMe, 17, 261
Watts, D. J., Larson, D., Marriage, T. A., et al. 2015, ApJ, 814, 103
Watts, D. J., Wang, B., Ali, A., et al. 2018, ApJ, 863, 121
Wei, T. 2012, Undergraduate thesis, The Johns Hopkins Univ.
Weiland, J. L., Odegard, N., Hill, R. S., et al. 2011, ApJS, 192, 19
Whitbourn, L. B., & Compton, R. C. 1985, ApOpt, 24, 217
Xu, Z., Brewer, M. K., Rojas, P. F., et al. 2020, ApJ, 891, 134
Zeng, L., Bennett, C. L., Chuss, D. T., & Wollack, E. J. 2010, Proc. SPIE, 7741, 774129
Zheng, Y. C., Tsang, K. T., Chan, K. L., et al. 2012, Icar, 219, 194